

# Adaptations for Wear Resistance and Damage Resilience: Micromechanics of Spider Cuticular “Tools”

Maryam Tadayon,\* Osnat Younes-Metzler, Yaniv Shelef, Paul Zaslansky, Alon Rechels, Alex Berner, Emil Zolotoyabko, Friedrich G. Barth, Peter Fratzl, Benny Bar-On, and Yael Politi\*

In the absence of minerals as stiffening agents, insects and spiders often use metal-ion cross-linking of protein matrices in their fully organic load-bearing “tools.” In this comparative study, the hierarchical fiber architecture, elemental distribution, and the micromechanical properties of the manganese- and calcium-rich cuticle of the claws of the spider *Cupiennius salei*, and the Zn-rich cuticle of the cheliceral fangs of the same animal are analyzed. By correlating experimental results to finite element analysis, functional microstructural and compositional adaptations are inferred leading to remarkable damage resilience and abrasion tolerance, respectively. The results further reveal that the incorporation of both zinc and manganese/calcium correlates well with increased biomaterial's stiffness and hardness. However, the abrasion-resistance of the claw material cross-linked by incorporation of Mn/Ca-ions surpasses that of many other non-mineralized biological counterparts and is comparable to that of the fang with more than triple Zn content. These biomaterial-adaptation paradigms for enhanced wear-resistance may serve as novel design principles for advanced, high-performance, functional surfaces, and graded materials.


Despite the limited number of natural building blocks, biological materials display a wide range of mechanical properties, achieved by hierarchical architecture and compositional gradients.<sup>[1]</sup> The cuticular exoskeleton of arthropods, the cuticle, consists of fibrous procuticle, composed of chitin-protein assembly, and an external fiberless epicuticle. The mechanical behavior of the cuticle as well as the structure of various organs and appendages (e.g., legs, wings, ovipositors, and fangs) were extensively studied in different arthropod groups among them insects, crustaceans, and spiders.<sup>[2]</sup> Here, however, we study the structure–property–function relationships in the tarsal claws of the spider *Cupiennius salei* and compare them to those in the fangs of the same species. The comparative approach allows us to identify material-level adaptations to a specific biomechanical function.

## 1. Introduction

Many biological “tools” such as claws, stingers, and mouthparts of animals have evolved to withstand repeated substantial mechanical loads, while performing various biomechanical functions such as piercing, grinding, cutting, and interlocking. At the nanoscale and microscale, these tools show structural and compositional variations that lead to localized stiffening and hardening of the biomaterial from which they are made.

The tarsal claws are small-scale biomechanical elements (“tools”) located distally on the legs of arthropods. They support various behaviors such as walking, climbing, and hanging by interlocking with structures on rough surfaces.<sup>[3]</sup> The spider fangs are mouthparts used to inject venom into the spider's prey by piercing through its exoskeleton. The claws and the fangs are made principally from the exoskeletal material of the spider, the cuticle. The fibers in the pro-cuticle are elongated  $\alpha$ -chitin crystals decorated by

Dr. M. Tadayon, Dr. O. Younes-Metzler, Prof. P. Fratzl, Prof. Y. Politi  
Department of Biomaterials  
Max Planck Institute of Colloids and Interfaces  
Potsdam 14476, Germany  
E-mail: Maryam.Tadayon@mpikg.mpg.de; Yael.Politi@mpikg.mpg.de  
Y. Shelef, A. Rechels, Prof. B. Bar-On  
Department of Mechanical Engineering  
Ben-Gurion University of the Negev  
Beer Sheva 84105, Israel

 The ORCID identification number(s) for the author(s) of this article can be found under <https://doi.org/10.1002/adfm.202000400>.

© 2020 The Authors. Published by WILEY-VCH Verlag GmbH & Co. KGaA, Weinheim. This is an open access article under the terms of the Creative Commons Attribution-NonCommercial License, which permits use, distribution and reproduction in any medium, provided the original work is properly cited and is not used for commercial purposes.

Dr. P. Zaslansky  
Julius Wolff Institut  
Charité—Universitätsmedizin  
Berlin 13353, Germany  
A. Berner, Prof. E. Zolotoyabko  
Department of Materials Science and Engineering  
Technion-Israel Institute of Technology  
Haifa 32000, Israel  
Prof. F. G. Barth  
Department of Neurobiology, Faculty of Life Sciences  
University of Vienna  
Vienna 1090, Austria  
Prof. Y. Politi  
B CUBE—Center for Molecular Bioengineering  
Technische Universität Dresden  
Dresden 01307, Germany

DOI: 10.1002/adfm.202000400

chitin-binding protein.<sup>[4]</sup> The chitin-protein fibers are aligned in sheets that stack on top of each other in either a parallel fiber arrangement (the long axes of the fibers in a sheet and in successive sheets are parallel), or as a twisted plywood structure,<sup>[5]</sup> where the fiber axis is rotated between sheets. The latter organization leads to a lamellar structure, in which a lamella is defined by a 180° rotation of the fiber axis.<sup>[6]</sup> Versatility in fiber architecture may lead to strong variations (orders of magnitudes) in the anisotropic mechanical properties of the (pro) cuticles in different body parts even within the same animal.<sup>[1c,7]</sup> Relationships between fiber orientation, stiffness, and biological functions have been repeatedly demonstrated in arthropods, in general,<sup>[8]</sup> and in the spider fangs, in particular.<sup>[2d,9]</sup>

In addition to architectural variations at multiple length-scales, the fangs of *C. salei* show local matrix reinforcement (hardening and stiffening) by Zn-His cross-linking.<sup>[2d]</sup> Indeed, varying the protein matrix composition and, especially, the manner in which it is cross-linked, is another way by which arthropods tune and adapt the mechanical properties of their cuticles. Mineralization is common in crustaceans; however, accumulations of Zn, Mn, and Ca are reported in other arthropods, especially in insects, in cuticular “tools” such as stingers, mandibles, and ovipositors.<sup>[10]</sup> Furthermore, in some cases, animals incorporate different metal-ions into different cuticular tools or different regions within the same

“tool.”<sup>[2a,10d]</sup> Available data indicate that metal-ion incorporation in fully organic biological materials can enhance their local mechanical properties, such as hardness, stiffness, toughness, and wear resistance to a level tantamount to that of some mineralized biological materials.<sup>[10j,11]</sup> Despite growing evidence for the mechanical importance of metal-ion cross-linking in biological materials, some important questions remain unaddressed, for example what is the effect of incorporating a certain metal ion over others.

While the structural-mechanical characteristics of various claws were extensively analyzed in a large-scale context (including contact force, hooking, and friction),<sup>[3,12]</sup> their biomaterial adaptation in terms of composition, nano- and micro-scale architectures, and mechanical properties have yet been studied. In the current research, we use finite element simulations to find critical locations of stress intensifications in the spider claw, and employ materials science methodology to identify possible adaptations of the claw biomaterial to these high-stress localizations. We find that the tarsal claws of the *C. salei* (Figure 1) are enriched with Ca and Mn-ions, and identify parallel fiber arrangement in the exocuticle, which is uncommon for fiber architecture in spiders. We demonstrate the effect of these features on the local and global mechanical properties of the claw. Finally, we analyze the biomaterial composition, architecture, and mechanical properties in

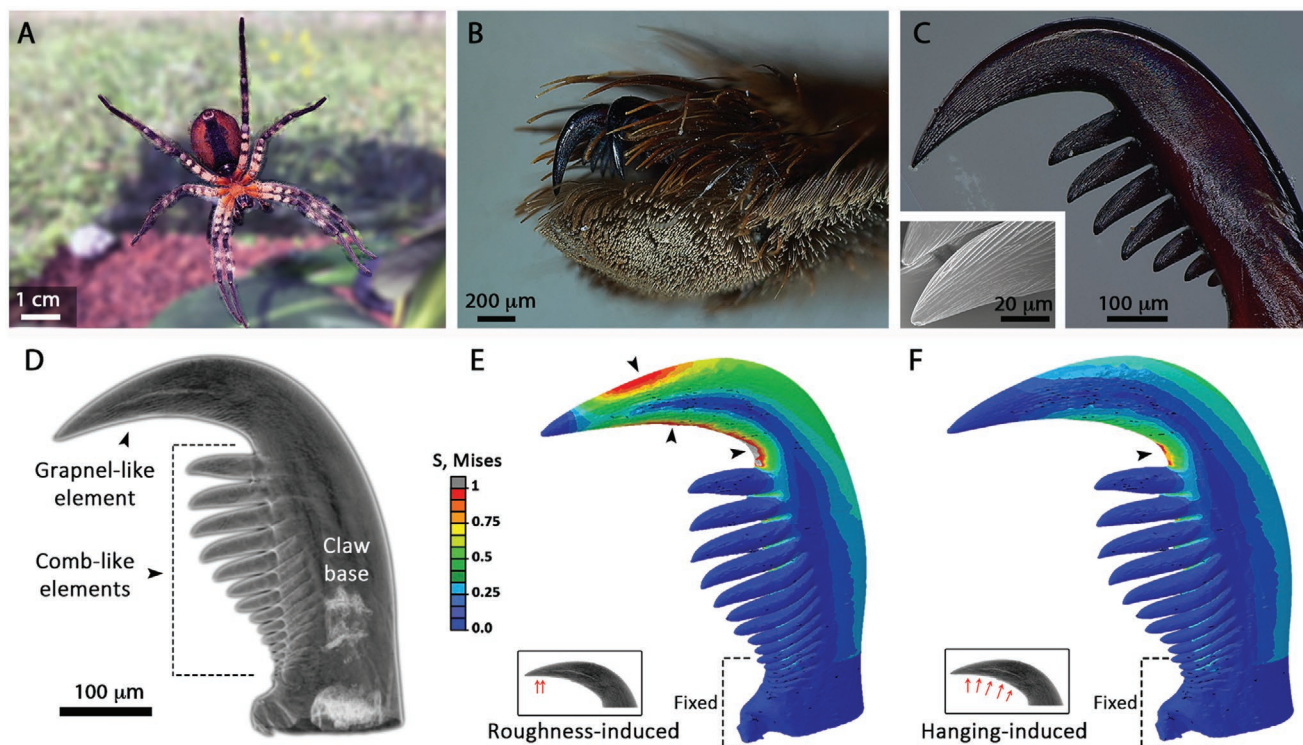


**Figure 1.** The tarsal claws of Central American wandering spider *Cupiennius salei* and FEA. A) Ventral view of a female spider resting on the glassy wall of a terrarium. B) Micrograph of a pair of spider tarsal claws and hair tufts at the end of the tarsus. C) Micrograph of a spider claw. The inset shows the SEM image of the tip of the claw and ridges on the surface. D) A volume rendering of the spider claw reconstructed from X-ray micro-CT data. The grapnel-like and comb-like elements are denoted. von Mises stress distribution maps of the claw at the two loading states, E) perpendicular loading applied to the near-tip-region, representing interlocking with surface roughness, and F) perpendicular loading applied at the mid-region of the element, representing hanging effects. Insets: Schematic description of the loading states. For each case, the von Mises stresses are normalized by the corresponding maximal stress. Sites of local maximal stress values are indicated by black arrowheads.

qualitative analogy and in quantitative comparison to the well-studied fang elements. Using this comparative approach, we discuss what appear to be materials adaptations to the specific functions of these two cuticular tools of the spider *C. salei*.

## 2. Results

### 2.1. Claw Morphology and Geometry

The tarsal claw of *C. salei* is shaped as a large grapple-like element (similar to the claws of the beetles) and a series of smaller comb-like elements (Figure 1). The claw is activated by two tendons connected to its base.<sup>[13]</sup> Two claws are positioned at the distal end of each tarsus (Figure 1B), and a third, smaller claw whose function is not clear, is located between them (not shown). Hereafter, the term “spider claw” refers to the two larger tarsal claws only. The geometrical form of the grapple-like element is curved and tapered similarly to that of the spider fang, but the inner contour of the grapple-like element approximately follows a quarter-perimeter of an ellipse rather than a circle.<sup>[9a]</sup> The surface of the claw shows ridges of various heights leading to increased surface roughness relative to the smooth distal part of the spider fang. These surface irregularities are more pronounced on the surface of the concave part of the grapple-like element.

### 2.2. Stress Distribution Upon Load

The response of the claw grapple-like element to functionally related loading states was investigated by finite element analysis (FEA). The simulations were conducted on a claw model, reconstructed from micro-CT data, employing a constant homogeneous elastic modulus (10 GPa, as measured by nanoindentation, see Section 2.5.1) (Figure 1D), by applying mechanical loads on the grapple-like region of the claw, keeping fixed boundary conditions on the proximal edge of the claw (proximal to the comb-like region). Two loading states were introduced: i) a roughness-induced loading state, for example, upon walking or standing, introduced by uniform pressure on the inner surface of the element close to its tip (Figure 1E), and ii) a hanging-induced loading state, for example, upon clinging onto vertical or inclined surfaces, introduced by pressure at the mid-region of the inner surface (Figure 1F). The resultant von Mises stress distributions<sup>[14]</sup> are depicted for the roughness-induced and hanging-induced loading states analyzed in Figure 1E,F. For both loading states, maximal stress concentrations (red-colored regions) are located at the base of the grapple-region; for the roughness-induced loading, high-stress regions are found also along the concave and convex sides of the grapple-like element. The comb-like elements experience no stresses, that is, they are unaffected by the roughness- and hanging-induced loadings, and are thus functionally irrelevant at these loading schemes.

### 2.3. Microstructural Characterization

The microstructure of the claw was initially studied using scanning electron microscopy (SEM) (Figure 2). Polished and etched

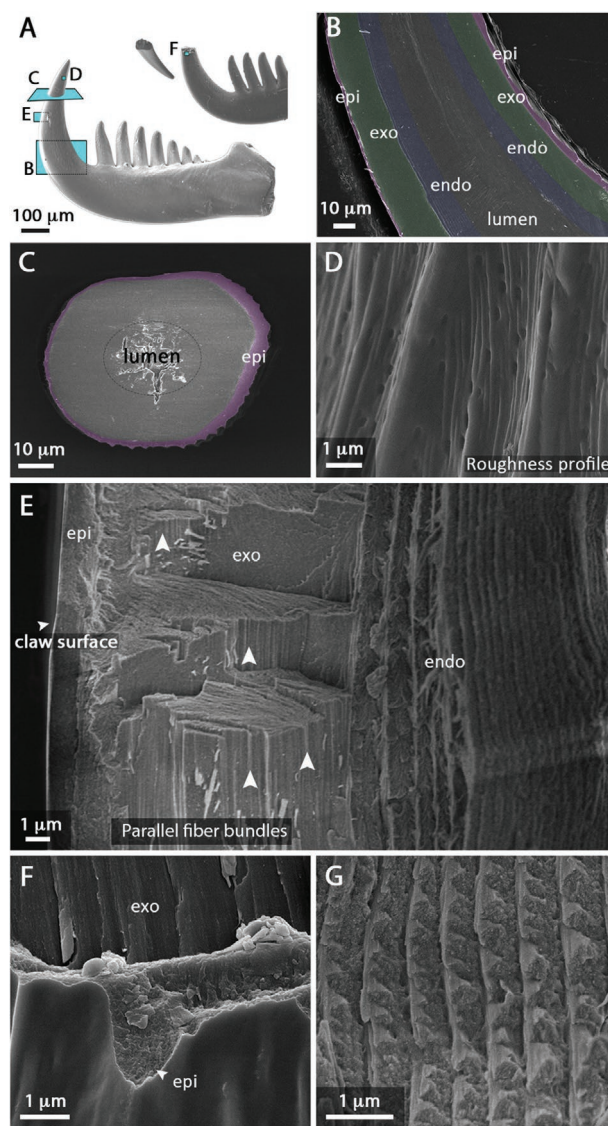


**Figure 2.** Scanning electron micrographs of the spider claw. A) An intact and a tip-broken claw used as a guide for the following micrographs. The cyan planes correspond to the orientation depicted in the corresponding panels. B) A polished and urea-etched longitudinal section of the base of the grapple-like element. The cuticular layers are highlighted: epicuticle in purple, exocuticle in green, and endocuticle in blue. C) A polished and urea-etched cross-section of the base of the grapple-like element. The epicuticle is highlighted in purple. The exo- and endocuticle layers are poorly resolved. D) The outer surface of the claw tip showing a rough profile and tiny openings attributed to nano-channel ending. E) A longitudinal fracture surface of the grapple-like element. The epi-, exo-, and endocuticle can be seen. F) A fractured pattern in the cross-section of the grapple-like element showing the epicuticle microstructure. A globular matrix in epicuticle and the parallel organization of fibers in the exocuticle are recognized. G) Lamellar structure of the endocuticle, forming a twisted plywood structure. The fracture pattern results from the continuous change in fiber orientation.

longitudinal and cross-sections from the base of the grapple-like element show the claw lumen as well as the epi-, exo- and endo (meso)-cuticle (Figure 2B,C). The fiberless epicuticle, highlighted by false color (purple), is both thicker ( $\approx 4\text{--}5\ \mu\text{m}$ )

and rougher (see Figure 2B–E and Figure S1, Supporting Information) in the concave part of the grapnel-like element than in its dorsal convex part ( $\approx 1 \mu\text{m}$ ). The maximum epicuticle thickness is observed at the tip ( $\approx 6\text{--}7 \mu\text{m}$ ). The ventral surface of the claw reveals elongated ridges of various heights leading to surface irregularities with different radii of protrusion. Numerous small openings with radii of tens of nanometers are also observed on the surface of the spider claw. The epicuticle nanostructure is roughly isotropic (Figure 2F).

The procuticle of spiders typically includes an exo- meso-, and endocuticle,<sup>[15]</sup> characterized by variable degree of cross-linking. In this study we do not distinguish between the meso- and endocuticle. The exocuticle, highlighted in green in Figure 2B, also shows varying thickness along the length of the claw. It is  $\approx 7\text{--}12 \mu\text{m}$  thick at the base of the grapnel-like element and  $\approx 4\text{--}5 \mu\text{m}$  in the comb-like elements (Figure S1B, Supporting Information). Longitudinal fractured surfaces close to the claw tip (Figure 2E) reveal that the exocuticle is built of densely packed fiber bundles oriented roughly parallel to the element's long axis. The fracture surface in cross-section displays a curved pattern (Figure S1C,D, Supporting Information), which presumably results from a variation in the fiber packing density in the radial and tangential directions (Figure S1E, Supporting Information). The endocuticle, highlighted in blue in Figure 2B, shows a typical lamellar structure of twisted plywood fiber arrangement (Figure 2E), where the sheets are parallel to the surface of the claw. The lamella thickness varies between  $\approx 400$  and  $800 \text{ nm}$  in the grapnel-like element. The microstructure of each comb-like element is

similar to that of the grapnel-like element where the layer thicknesses are reduced.

Scanning small- and wide-angle X-ray scattering (SAXS/WAXS) measurements across the entire claw provide further information on the chitin-protein nanofibrils arrangement (Figure 3). The 2D scattering patterns (Figure 3A) reveal a pronounced SAXS signal around scattering vector,  $q = 1.2\text{--}1.3 \text{ nm}^{-1}$ . The SAXS signal is assigned to inter-fibrillar diffraction, resulting from the close-packed chitin nanofibrils ( $d$ -spacing =  $2\pi/q$ , where  $q$  is the scattering angle). The azimuthal intensity distribution of the SAXS signal brings information about the degree of co-alignment of the chitin-protein fibrils and their spatial orientation. Both parameters are mapped in Figure 3. The dark lines indicate the main orientation of the chitin fibers, and their length is proportional to the relative degree of fiber co-alignment at every point. Throughout the entire claw, a large fraction of the fibers is orientated parallel to its long axis. Along the outer layers, especially along the concave side of the grapnel-like element, the fibers are also highly co-aligned.

A map of the fiber-to-fiber distance,  $d$ , deduced from the  $q$ -dependence of the scattering intensity, is presented in Figure 3C. The chitin content in volume fraction,  $\phi_c$ , has been calculated from the inter-fiber distance assuming constant fibril diameter and a hexagonal close packing of the fibers (see Experimental Section and Figure 3D). The chitin volume fraction varies between 0.27 and 0.36. Chitin dense regions ( $d \approx 4.9 \pm 0.1 \text{ nm}$  or  $\phi_c \approx 0.34 \pm 0.01$ ) are localized at the outer layers of the concave side of the grapnel-like element, at the

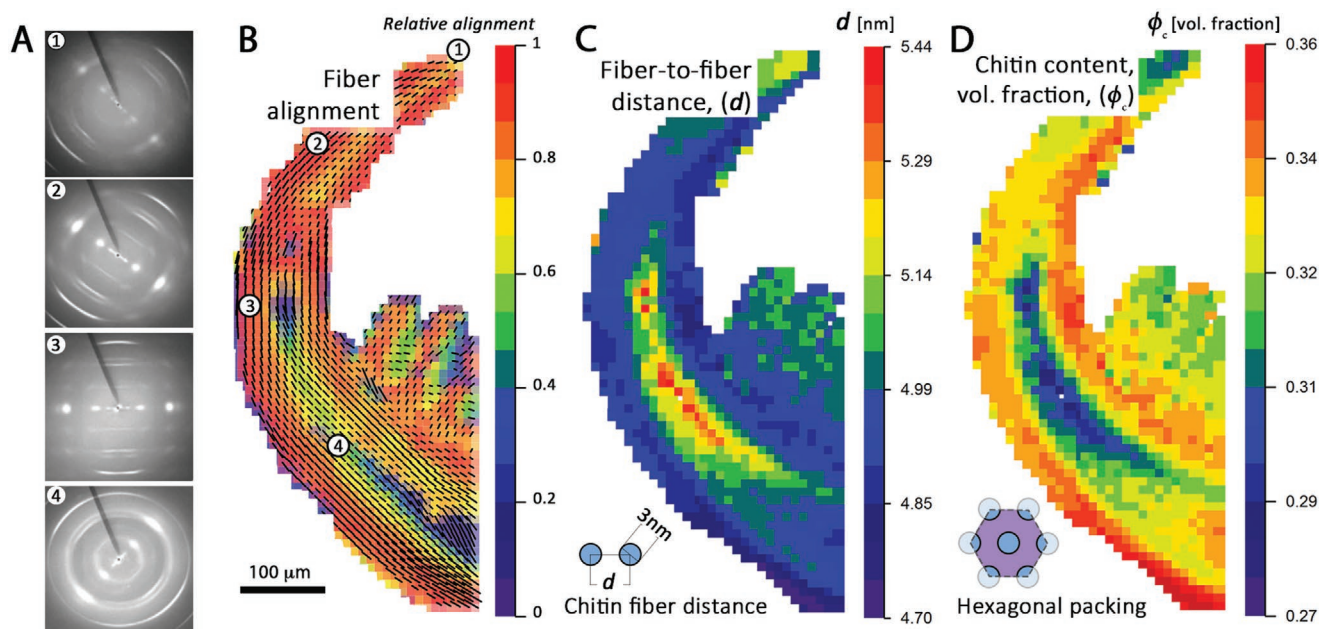


**Figure 3.** Microstructure of the spider tarsal claw evaluated from small-angle X-ray scattering (SAXS). A) 2D patterns of the fibrous texture in different regions, depicted in panel B and exemplifying the variation in chitin orientation and alignment. B) The relative degree of fiber alignment based on SAXS measurements. The length and orientation of each vector reflect the normalized relative degree of alignment and the long-axis orientation of the fraction of aligned fibers, respectively. The colors (arbitrary scale) represent the relative width of the integrated SAXS intensity in azimuthal space as a measure of the degree of fiber alignment. Highest degree of fiber alignment corresponds to the minimum peak widths (red); blue color represents the maximal peak width, corresponding to minimum degree of fiber alignment. C) Color map of the fiber-to-fiber distance (in nanometer) calculated from the SAXS radial peak position in reciprocal space ( $q$ -value). D) Chitin content calculated from the fiber distance assuming hexagonal packing (color code: chitin vol. fraction). Note that there is an inverse correlation between the chitin fiber distance and chitin fiber density.

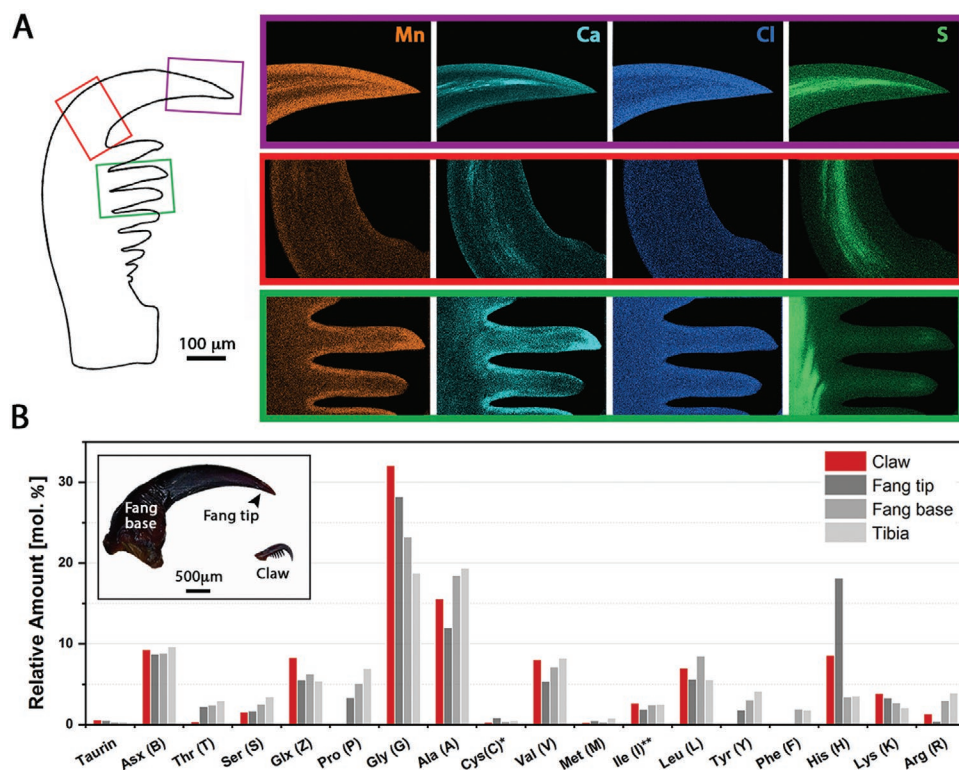


**Figure 4.** Chemical composition. A) High-resolution EDS elemental maps of polished claw sections in the regions, marked by the same color boxes, as on a claw sketch (left). The manganese (Mn, orange), calcium (Ca, cyan), chlorine (Cl, blue), and sulfur (S, green) distribution maps showing site-specific gradients. Arbitrary color scale is the same between regions for each element. B) Amino acid composition of the spider tarsal claw (see red bars) in comparison with those of the fang (tip and base<sup>[24,9]</sup>) and walking leg tibia (gray bars). Note the enrichment of Glx, histidine, and hydrophobic residues in the claw. No tryptophan (Trp) (whose retention time is between Lys and Arg) was detected. \*Cys represents Cys, Cys2, and Cys (O<sub>3</sub>H). \*\*Ile and allo-Ile are not differentiated.

bases of the comb-like elements, and at the outer layers of the claw dorsal part (close to the claw base). Chitin packing is less dense close to the tips of the grapnel- and comb-like elements ( $d \approx 5.1 \pm 0.1$  nm, and  $\phi_c \approx 0.31 \pm 0.01$ ).

## 2.4. Chemical Composition

### 2.4.1. Degree of Sclerotization

Sclerotization refers to the covalent cross-linking of the protein matrix by catechol derivatives through various enzymatic pathways.<sup>[16]</sup> The epi- and exocuticles of arthropods are usually hardened and stiffened by sclerotization. The process involves dehydration and often correlates with amber to dark brown coloration (hence it is also referred to as tanning). The outer layers of the claw are tanned relative to the endocuticle, with darker coloration appearing at the tip of the grapnel-like element and at the connecting regions between the comb-like elements (Figure S2, Supporting Information).

### 2.4.2. Elemental Composition

Energy-dispersive X-ray spectroscopy (EDS) and wavelength-dispersive X-ray spectroscopy (WDS) were used to study the

elemental distribution across the claw. In addition to the expected elements, such as C, O, and N, we found a significant amount of Mn, Ca, Cl, and S throughout the claw, as well as Zn in the fang. Impurity distributions in claw are qualitatively presented in the form of maps, showing brighter contrast for higher element concentration (Figure 4). The results of point-to-point quantitative analysis in claw and fang are summarized in Figure S3, Supporting Information.

Sulfur is concentrated in the claw lumen at  $\approx 0.47$  at% (Note S1, Supporting Information), while Cl is spread more evenly throughout the sample with an approximate concentration of  $0.20 \pm 0.09$  at%. A slightly higher content of Cl is observed at the tip of the grapnel-like element. Mn and Ca-ions co-exist with higher concentrations in the outer layers of the grapnel-like element and up to 15  $\mu\text{m}$  beneath the surface, which corresponds to the epi- and exocuticle. The concentrations of Mn and Ca in the outer layers of the grapnel-like element are  $0.4 \pm 0.1$  and  $0.6 \pm 0.1$  at%, respectively; however, the Ca-to-Mn atomic ratio is not constant across the claw. It is 0.3:1 in the lumen, and varies from 0.7:1 to 2.4:1 in the outer layer of the grapnel-like element and the claw base. The maximum amounts of Ca and Mn in the claw were detected in the epicuticle and the tip of the grapnel-like element to be  $\approx 0.9$  and 0.7 at%, respectively (Figure S3, Supporting Information). X-ray fluorescence (XRF) measurements confirm the EDS and WDS results and, in addition, show traces of Br, Mg, K, and Na (data not shown).

EDS and WDS analyses were also performed for the fangs of *C. salei* (Figure S3, Supporting Information). In the fang, Zn and Ca are present at separate locations, whereas Zn and Cl co-localize. The maximum amount of Zn was found to be  $\approx 5.6$  at% in the tip epicuticle, far more than the maximum detected total concentration of Mn and Ca in the claw tip ( $\approx 1.6$  at%).

#### 2.4.3. Mn Chemical State

To probe the interaction of Mn-ions with protein matrix and to determine the chemical state of Mn and its coordination geometry, we used Mn K-edge X-ray absorption near edge spectroscopy (XANES) (Figure S4, Supporting Information). The edge position (defined as the first maximum in the derivative of the x-ray absorption spectrum) indicates a divalent oxidation state of Mn-ions within the native claws, and the line shape of the Mn K-edge spectrum indicates disorder in the short-range around the Mn-ion. Micro-focused XANES showed no variation in the Mn K-edge position or line-shape in the cuticle with respect to that in the lumen (Figure S4, Supporting Information).

#### 2.4.4. Protein Composition

Quantitative amino acid analysis (AAA) was applied to find chemical composition of the proteins within the claw

(Figure 4B). The results are compared with the amino acid content of *C. salei* fangs (tip and base)<sup>[2d]</sup> and walking leg tibiae. We find a high content of hydrophobic residues such as glycine (Gly, 32.1 mol%), alanine (Ala, 15.6 mol%), and valine (Val, 8.1 mol%). Aspartate/asparagine (Asx) and glutamate/glutamine (Glx) are also relatively abundant, accounting for 8.3 and 8.7 mol%, respectively. Importantly, the presence of a large amount of histidine (His, 8.6 mol%) is observed. Although this amount is lower than the His content in the tip of the spider fang, it is much higher than its content in the fang base<sup>[2d]</sup> and in the tibia.

### 2.5. Mechanical Properties

#### 2.5.1. Nanoindentation Analysis

Metal-ion incorporation into the cuticle matrix and structural anisotropy play important roles in determining mechanical properties of the material.<sup>[11b]</sup> In order to correlate between a material's structure, composition, and mechanical properties, we applied nanoindentation at selected regions on longitudinal sections of the claw in dry and hydrated conditions (Figure 5). The results show a gradual variation in both reduced moduli,  $E_r$ , and hardness,  $H$ , throughout the claw with highest magnitudes at the tip of the grapnel-like element and high levels at its outer layers (Figure 5A). The reduced modulus and hardness mean values from grapnel-like element are summarized in Table 1. In hydrated state, as compared to the dry condition

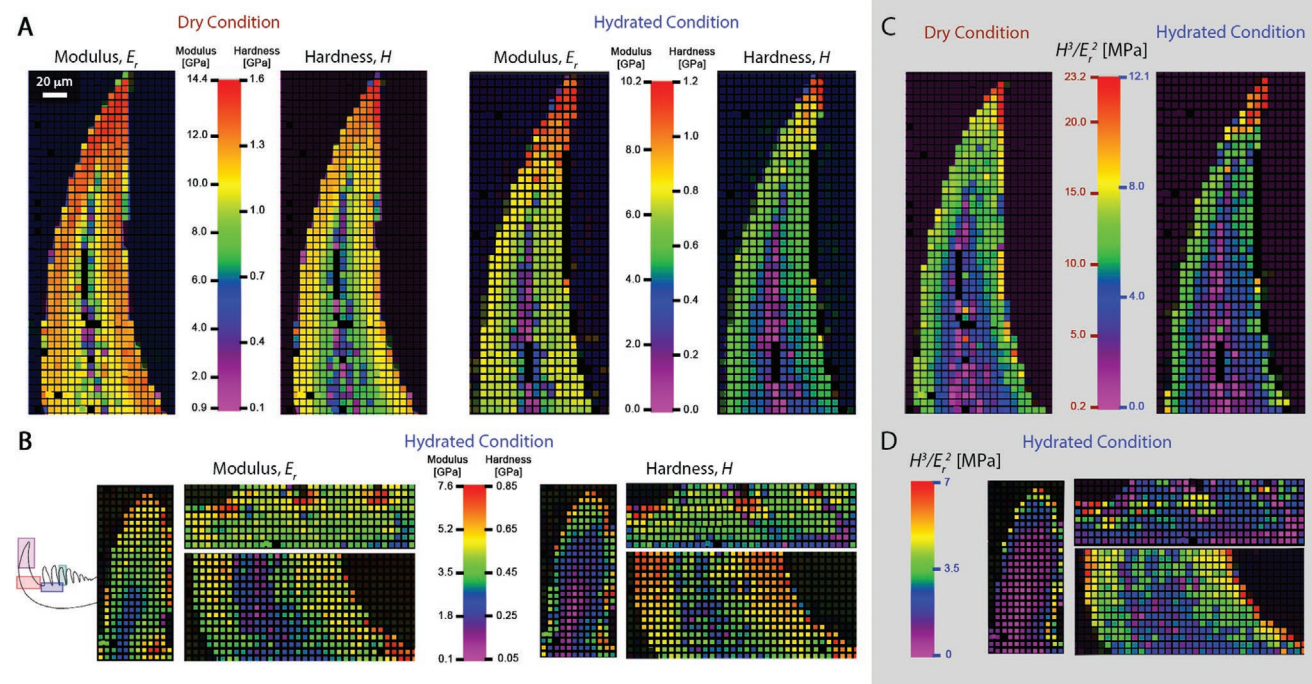


**Figure 5.** Micromechanical properties obtained by nanoindentation. A) Nanoindentation maps of reduced modulus ( $E_r$ ) and hardness ( $H$ ), obtained with 5  $\mu\text{m}$  indentation steps on a longitudinal section of the grapnel-like distal element of the spider claw, in dry (left) and hydrated (right) conditions. B) Nanoindentation maps on a comb-like element, base of the comb-like elements, and the base of the grapnel, obtained with the same measurement setup as in panel A, for hydrated condition. Results show graded mechanical properties in these regions. C) Maps of the ratio,  $H^3/E_2^2$ , calculated from panel A in dry (left) and hydrated (right) condition. D) The calculated ratio of  $H^3/E_2^2$  for regions shown in panel B.

**Table 1.** Nanoindentation modulus and hardness of a grapnel-like element probed on a longitudinal section.

Distance from the outer surface	Reduced modulus, $E_r$ [GPa]		Hardness, $H$ [GPa]	
	Dry	Hydrated	Dry	Hydrated
At the tip (up to 20 $\mu\text{m}$ ) <sup>a)</sup>	14.0 $\pm$ 0.4	9.9 $\pm$ 0.3	1.52 $\pm$ 0.14	1.13 $\pm$ 0.10
$\approx$ 5–15 $\mu\text{m}$ <sup>b)</sup>	12.1 $\pm$ 0.8	7.0 $\pm$ 0.9	1.21 $\pm$ 0.24	0.65 $\pm$ 0.04
$\approx$ 15–25 $\mu\text{m}$ <sup>c)</sup>	10.7 $\pm$ 0.9	4.3 $\pm$ 0.9	0.91 $\pm$ 0.07	0.34 $\pm$ 0.08

<sup>a)</sup>The data from the tip represents the metal-rich fiberless epicuticle and the metal ion-rich exocuticle where the fiber density is low; <sup>b)</sup>This region corresponds to the metal ion-rich outer layer of the procuticle where the microstructure contains parallel fiber arrangement. The fibers are parallel to the section surface; <sup>c)</sup>The area corresponds to the inner layers of the procuticle with lower metal-ion content and a helicoidal fiber organization.

the modulus drops  $\approx$ 1.4-fold, 1.7-fold, and 2.5-fold for the tip, the outer layer and inner layer of the grapnel-like element, respectively. Thus, the inner layers of the claw show a larger reduction in the measured mechanical properties relative to the outer layers and the tip upon hydration. Similar maps on other regions of the claw, including the base of the grapnel-like element, the comb-like element bases, and a comb-like element also display graded mechanical properties both in dry and hydrated conditions (Figure 5B), with increasing  $E_r$  and  $H$  in regions predicted by FEA to serve as stress concentrators.

In order to better understand the contribution of metal-ions to the mechanical properties of the claw cuticle, we chelated the metal ions from the surface of claw cross-sections (cut  $\approx$ 120  $\mu\text{m}$  away from the tip) using EDTA, as suggested by Broomell et al.<sup>[17]</sup> Reduced modulus and hardness maps were obtained by nanoindentation under dry conditions, and the metal-ion concentration was estimated by elemental analysis using EDS. Chelating the metal-ions with EDTA ( $\approx$ twofold drop in Mn and Ca concentrations) leads to a drop of both the reduced modulus and the hardness to almost half the original value (Figure S5, Supporting Information). Partial recovery ( $\approx$ 75%) of the measured mechanical properties was obtained by soaking the EDTA treated samples in  $\text{MnCl}_2$  solutions (resulting in partial Mn recovery). Using  $\text{ZnCl}_2$  solution instead led to Zn incorporation at the expense of Ca and Mn-ions, and leading to partial ( $\approx$ 65%) recovery of the measured mechanical properties (Figure S5, Supporting Information). Mn and Zn K-edge XANES analysis of the samples with reintroduced metal-ions reveal that the metal environment is similar, and that no inorganic salts precipitated in the reconstituted samples (Figure S4E,F, Supporting Information). These measurements demonstrate the link between metal-ion coordination and increased hardness and stiffness, and that the same protein matrix can interchangeably incorporate Mn and Zn as also observed in *Nereis* jaws.<sup>[17]</sup>

### 2.5.2. Wear-Resistance Analysis

The ratio,  $H^3/E^2$ , is customarily employed to characterize the wear resistance of a material.<sup>[18]</sup> As an initial estimate of the wear-resistance of the claw material we plotted this ratio based on the indentation values in dry and hydrated conditions (Figure 5C,D). Clearly, the external layers of the grapnel-like element and, especially, its tip exhibit higher ratios than the internal layers suggesting a correlation between metal-ion incorporation and an increase in wear-resistance. Note that the regions exhibiting higher wear resistance are located at

the extremities of the sample and are thinner (equal to one-two indentation data points, that is, around 5–10  $\mu\text{m}$ ) than the regions exhibiting increased  $E_r$  or  $H$  (around four indentation points across, i.e., being nearly 20  $\mu\text{m}$  thick).

At the next stage nanowear tests were conducted at different regions along *C. salei* claw epicuticle in regions that contain or lack metal-ions. Similar tests were conducted on the fangs of *C. salei*, to provide a comparative analysis between these two “tools.” Using a 1  $\mu\text{m}$  conical nanoindenter tip and a 2D force transducer we examined the wear resistance of Mn/Ca-rich and metal-poor regions of the claw, as well as Zn-rich region of the spider fang. Nanowear test comprises scratching a surface multiple times with a predefined vertical load of the indenter tip. To identify the wear resistance, the mean worn depth is determined using post-wear scanning probe microscopy (SPM) (see Experimental Section). The mean worn depth is similar in the Mn/Ca containing epicuticle of the claw and the Zn-rich epicuticle of the fang, that is, 21.4  $\pm$  7.3 nm, 30.8  $\pm$  8.2 nm, respectively. However, pre- and post-wear elemental distribution analysis performed at the same regions showed 0.36 and 0.6 at% for Ca and Mn, respectively, (or 0.96 at% in total) in the claw, and 5.6 at% Zn in the fang. As the epicuticle is thinner (less than 1  $\mu\text{m}$ ) in metal-depleted regions, we were unable to perform wear-test on a cross-section. Therefore, we probed the claw outer surface at the base where it is considerably smooth relative to the grapnel surface (Figure 6A). The roughness of the tested surfaces was initially evaluated by pre-SPM. Due to the nanoindenter tip movement confinements and due to the thinner epicuticle in this region (less than 1  $\mu\text{m}$ ), the experiment was performed with only 10 sliding cycles whereas all other tests were set to 30 sliding cycles, but the amount of worn material in the low-content metal region was nevertheless significantly higher (460  $\pm$  89 nm) (Figure 6B).

## 3. Discussion

Spiders are capable to attach and walk on diverse natural substrates, from rough to smooth and slippery surfaces. This is most likely achieved by the synergistic function of claws and cuticular hair tufts.<sup>[8d]</sup> Attachment to smooth surfaces is very well understood. It involves a large number of hairs (Figure 1B) with soft spatulate tips that allow multiple molecular scale interactions such as van der Waals forces between the attachment hairs and the smooth surface.<sup>[19]</sup> At large roughness scales, however, the hairy structures are not efficient and the claws (Figure 1C) are used instead interlocking with the

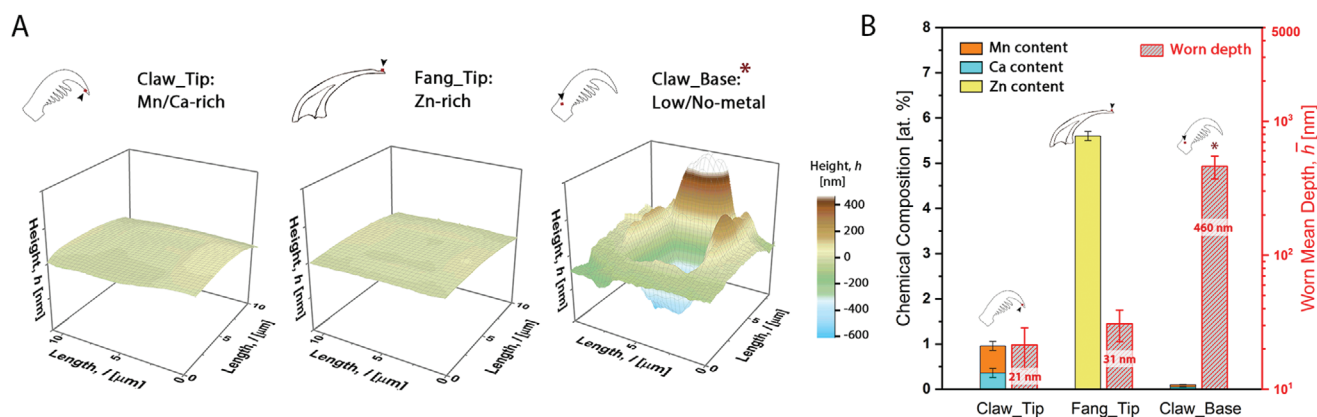


**Figure 6.** Correlation between wear resistance and metal coordination. A) Post-wear scanning probe imaging (SPM) on “epicuticular” zones of the spider claw and fang, where no chitin fibers exist. Insignificant wear is seen in Mn/Ca-rich zone on the claw tip (top panel), and Zn-rich zone on fang tip (middle panel) as compared to the low metal-containing zone on the claw base (bottom panel). B) The bar chart representing the mean worn depth and the corresponding metal-ion composition for the zones in panel A. \*Note that the number of nanowear sliding cycles performed on the low-metal region was 10 instead of 30 in other regions.

surface features. This mechanism is largely driven by frictional forces.<sup>[3]</sup> The epicuticle surface irregularities, specifically on the concave part of the grapnel-like element, are thus expected to increase the friction between the claw and the substrate, thus to play an important role for locomotion by securing the attachment and clamping onto the rough substrates.<sup>[12b]</sup> Rough surfaces have higher friction coefficients than smooth surfaces and are more prone to wear.<sup>[20]</sup> It is therefore not surprising that the epicuticle in the concave part of the grapnel-like element is thickened and shows increased wear resistance. The thinner epicuticle in the convex dorsal region is not involved in interlocking and shows lower roughness.

Typically, arthropod cuticles reveal a microscale layered arrays, exo- and endocuticle, with nanocomposite architectures in the form of rotated plywood structure.<sup>[8f]</sup> Parallel fiber architecture, which are less widespread, appears often (but not always, e.g., ref. [21]) in cuticle structures which require tensile and/or bending-resistance (e.g., tendons,<sup>[4c]</sup> fang,<sup>[9a]</sup> and attachment setae).<sup>[8d]</sup> While the rotated plywood architecture provides equivalent resistance to bending and torsion loadings, the parallel fiber architecture provides superior resistance to bending, but much inferior resistance for torsion.<sup>[6,8e]</sup> In the fang, the parallel fiber organization is sandwiched between two rotated plywood layers, whereas in the claw, it occupies the entire exocuticle cross-section along the grapnel-like and the comb-like elements (Figure S6, Supporting Information). From a comparative mechanical–functional viewpoint, the roughness- and hanging-induced loadings of the claw generate merely planar force states, yet the biting-induced loadings of the fangs generate in addition non-planar forces (determined by the fang and the target). Accordingly, both the claws and the fangs accommodate significant bending loads during their natural function, but the fangs also have to accommodate twisting loads that are not present in the claws (see Figure S6, Supporting Information). Consequentially, the parallel fiber exocuticle of the spider claw may be viewed as a biomaterial adaptation to resist its bending-dominant functional loads; likewise, the alternating plywood/parallel fiber arrangement in the cuticle of the spider fang may be viewed as a biomaterial

adaptation to resist combined bending–torsion functional loads.<sup>[9a]</sup> Indeed, the chitin volume fraction is highest in the outer layers of the concave central part of the claw grapnel-like element, where tensile stress is expected upon loading.

The amino acid composition of the claws is similar to that of the fangs. The coexistence of a high amount of Gly and Ala in hardened/stiffened protein matrices also seen in the fang is thought to endow them with increased stiffness by promoting  $\beta$ -sheets formation.<sup>[22]</sup> In *C. salei* fangs His and Zn co-localize and have been shown to bind via coordination bonding. As we are unable to isolate the metal-rich regions from the rest of the claw (due to its small size), we cannot unequivocally determine the relationship between the protein composition and the presence of metal-ions. However, given the high relative abundance of His in the claws protein matrix, and given the similarity of the XANES spectra of the native materials as well as those of the metal ion exchange experiments, in which Zn is substituted with Mn in the fangs and Mn/Ca ions are substituted with Zn ions in claws, it is likely that His is involved in the Mn binding, possibly together with other residues (e.g., Asx and Glx which also occur in elevated levels) in the claw. Indeed, the Mn K-edge XANES data show that the ion environment is disordered and may therefore accommodate a variety of ligands.

We find correlation between areas with increased values of  $E_r$  and  $H$  and regions, which according to FEA work as stress concentrators upon load. The increased mechanical responses in different regions of the spider claw are attributed to the combination of few parameters, such as the orientation and alignment of the chitin fibers, the localization of different proteins, degree of sclerotization and metal-ion content. The effect of fiber orientation is exemplified by comparing the nano-indentation results of cross- and longitudinal sections of the exocuticle in the grapnel-like element. At the same region, about 120  $\mu\text{m}$  away from the tip, we measured  $\approx 13.5$  GPa for  $E_r$  in longitudinal section where the fibers are parallel to the section surface (see Figure 5A, modulus map for dry sample) and  $\approx 17$  GPa in the cross-section where the fibers are perpendicular to it (Figure S5, Supporting Information).



Metal-ion cross-linking of proteinaceous matrices is well known in biological materials.<sup>[10a-c,f,g,11b,23]</sup> It has been repeatedly demonstrated that the incorporation of metal-ions leads to increased mechanical properties such as indentation hardness, indentation stiffness and wear resistance. It has also been shown that the well-documented drop in mechanical response of biopolymers due to hydration is reduced in the presence of metal-ion cross-linking.<sup>[24]</sup> The nanoindentation results reported here are consistent with these observations. According to the nanoindentation results reported here and in ref. [2d] the Zn reinforced regions in the fang show a higher elastic modulus than the Mn/Ca-containing regions of the claw. At least in part, this effect may be related to the higher (more than triplicate) local concentration of Zn in the fang relative to the total local amount of Mn and Ca in the claw. Hardness, however, is increased in the Ca/Mn regions of the claw, as compared to the Zn-rich regions in the fang. Therefore, when considering the enhancement of wear-resistance, it seems that the incorporation of Mn/Ca is more efficient than the incorporation of Zn-ions (Figure 7). For the spider fang, the values of  $H^3/E^2$ , obtained in dry longitudinal sections, are around 5 MPa (in Zn-rich region), 3.5 MPa (in Ca-rich region), and 1.2 MPa in metal-depleted regions. In case of the tarsal claw, the value of  $H^3/E^2$  reaches 20 MPa for metal (Ca/Mn)-rich epicuticular regions and 5 MPa for regions devoid of metal-ions. These values are based on the indentation experiments with dry material. The hydrated claw still shows a high ratio,  $H^3/E^2 \approx 10$  MPa, in the metal-rich zone, which is even higher than that of the fang in dry condition. The modulus and hardness of the claw and fang, and their estimated “abrasion resistance” determined

by the ratio of  $H^3/E^2$ , are compared with those of other biogenic materials, using Ashby plots<sup>[25]</sup> (Figure 7). The abrasion tolerance of the claws is higher than that of many fully-organic counterparts such as the squid beak<sup>[26]</sup> and the Zn-rich *Nereis* jaw<sup>[10b]</sup> and comparable even with some highly mineralized matrices such as enamel and nacre.<sup>[11a,27]</sup>

Moreover, the nanowear test results show that the incorporation of metal-ions can increase the wear-resistance of the material compared to regions without incorporated metal-ions. We observed similar wear (worn depth of  $\approx 20\text{--}30$  nm) for Zn-rich regions in the fang and the Ca/Mn-rich regions in the claw, but Zn-ion concentration in the former is more than triple the total concentration of Mn/Ca-ions in the latter. At the moment, we cannot unequivocally determine whether this effect is solely the result of the metal-ion crosslinking or yet another still un-identified composition variant. However, the results of the metal-substitution experiments support the hypothesis that incorporation of Mn/Ca ions may be more efficient in increasing wear-resistance than Zn ions. At the atomic scale, the elastic properties of the material are correlated to the number and distribution of chemical bonds within the matrix. Hardness, on the other hand, describes the plastic deformation of the material and therefore requires breaking of chemical bonds. Consequently, it depends not only on the density of crosslinking, but also on their strength. Based on the XANES results we predict that the coordination number around the Zn and Mn ions in the respective cuticles is similar, and therefore we expect three times more coordination bonds in the Zn-rich fang matrix relative to the Ca/Mn rich claw matrix leading to higher stiffness (see Figure S7, Supporting Information),

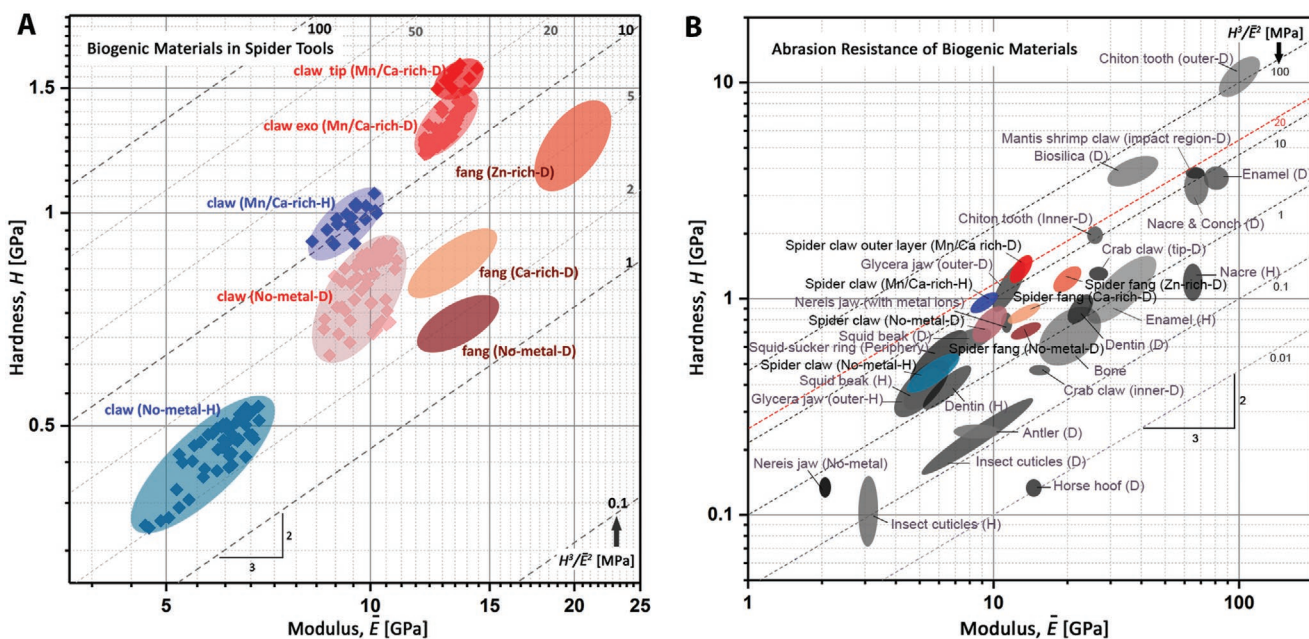


**Figure 7.** Evaluation of the spider claw mechanics compared with that of the spider fang in Ashby plots (with log-log scale) based on their resistance against yielding. A) The property map representing hardness versus elastic modulus of the spider claw and the fang, comparing locations with different metal-ion content. The claw tip data are mainly collected from  $\approx 20$   $\mu\text{m}$  from the tip, while the claw exo is attributed to the measurement on the outer layer up to  $\approx 100$   $\mu\text{m}$  from the tip in the grapple-like element. B) Comparison between the spider tools with biological tools of other animals having “no/low” to “high” mineral content.<sup>[10,11]</sup> The characteristic lines are representative for the wear resistance of the materials. D: dry conditions; H: hydrated conditions.

whereas the higher hardness in the claw may be understood by proposing stronger coordination bonds for Mn-ions relative to Zn-ion in the epicuticular matrices of the claw and fang, respectively. Density functional theory (DFT)<sup>[28]</sup> studies of the mechanics of different metal-catecholate complexes have shown that the Mn-O bond is almost two times stronger than Zn-O due to increased covalent nature of Mn-O coordination relative to the latter. In the same report, however, a lower binding strength was determined for the Ca-O bond due to its mainly-ionic nature.<sup>[28]</sup> As we have not determined the nature of the ligands in our system, we can only speculate that the strength and the total number of the coordination bonds in the matrix are at the base of our mechanical observations. Further studies and the development of molecular models are required to clarify this point.

First attempts in translating concepts derived from the study of biological materials and specifically metal-ion cross-linking, in hydrated and anhydrous polymeric matrices show great promise. Iron-catechol interactions allowed pH-induced self-healing in polymeric hydrogels,<sup>[29]</sup> whereas they promoted toughening and increase stiffness to dry elastomers while endowing the material with restorable ability to dissipate mechanical energy.<sup>[30]</sup> Gaining understanding of the use of other types of metal-ion cross-links in nature is bound to allow better tuning of the materials properties to function.

#### 4. Conclusion

Similar to the fangs of the spider *C. salei*, its tarsal claws show multi-scale structural and compositional gradients that endow them with mechanical properties adapted to their specific functional necessities. The microstructural motives vary between the fangs and the claws in a manner that reflects their respective biological functions. Fiber orientation, chitin volume fraction, and the level of cross-linking, as determined by cuticle sclerotization (tanning), as well as metal-ion distribution correlate well with FEA-predicted stress distribution. Local metal-ion incorporation into the cuticle enhances its overall mechanical properties such as indentation hardness, stiffness, and wear-resistance. We found that higher concentration of Zn in the spider fang leads to the increased material stiffness, whereas increased levels of Mn/Ca in the claw lead to improved hardness and wear resistance. Understanding the ways by which organisms build functional materials, may lead to optimized strategies for biologically inspired material design.

#### 5. Experimental Section

**Spider Specimens and Sample Preparation:** Alive fully matured specimens of the Central American wandering spider *C. salei* (Figure 1A) were obtained from the breeding stock of the Department of Neurobiology of the University of Vienna. The spiders were freshly frozen and the claws were dissected away from the tarsus and kept frozen prior to their usage.

Isolated claws were immersed in methylmetacrylate (MMA) for 8 h and polymerized in the oven at 60 °C. For SEM investigation, fractured or embedded and polished samples were used. For the latter case, the samples were treated in 8 m UREA/5% acetic acid solution for 30 s.

The samples were then mounted on the conductive carbon tapes and sputtered with Pt to avoid surface charges. For the synchrotron XANES and XRF measurements, the sample was glued onto a substrate and cut in ≈10 μm-thick slices using a vibratome device (Leica VT1000 S), while keeping it hydrated all the time. The samples were then high-pressure frozen, using Leica EM HPM100, and kept in the liquid nitrogen prior to measurements. For optical microscopy, nanoindentation/nanowear, and EDS, longitudinal sections or cross-sections of the embedded samples were ground and finely polished down to 0.5 μm until the desired region was reached. The nanoindentation/nanowear measurements were followed by EDS and WDS analyses on the same regions in the same samples. For the nanoindentation measurements of chelated and metal re-substituted samples, a microtomed (Leica SM2500E, Leica Microsystems, Bensheim, Germany) cross-section was used to access the same positions of the claw tip (≈30 μm from the tip). This was achieved by cutting ten slices (each slice being ≈3 μm thick) from the tip of the claw. For elemental analysis and nanoindentation on the sample cross-section, either the whole claw or embedded samples were subjected to metal chelation procedure and, later on, to the metal-ion replacement of the same or another metal-ion. For this purpose, the specimens were submerged in 50 mM Tris/200 mM EDTA, pH 8, incubated in sealed vials, while stirring for 4 days at room temperature, as suggested by Broomell et al.<sup>[10b]</sup> After that, they were rinsed thoroughly in 50 mM Tris-Cl (pH 8) and Milli-Q water for 12 h prior to experiments. For Mn and Zn re-constitution, pre-depleted samples were incubated, respectively, in 100 mM MnCl<sub>2</sub> (Sigma-Aldrich) or ZnCl<sub>2</sub> (Sigma-Aldrich) for 72 h at room temperature. Then, they were rinsed in Milli-Q water for 12 h before experiments.

**Micro-Computed Tomography:** For monochromatic absorption-contrast micro-computed tomography (Micro-CT), a dry claw was mounted upright on the rotating stage of the microtomography setup of the BAMline imaging beam line of BESSY II storage ring (HZB: Helmholtz Center Berlin for Materials and Energy). About 900 radiographs were recorded at angular increments of 0.3° using an X-ray energy of 20 keV ( $\Delta E/E = 0.5\%$ ) in absorption mode. The projection images had an effective pixel size of 0.792 μm and were normalized and reconstructed using the ESRF python code PyHST (ESRF, Grenoble, France). They were then visualized, rotated, and cropped (Amira 5.1, Visage Imaging GmbH, Germany).

**Finite Element Analysis:** Reconstructed cross-sectional images of the major grapnel-like element of the spider claw, obtained by X-ray micro-computed tomography, were implemented into Avizo software (9.4) to extract the geometrical parameters of the element. Commercial FEA software (ABAQUS/explicit 6.19) was used for the numerical simulations. The major grapnel-like element of the spider claw was modeled as isotropic material with an elastic constitutive behavior (realized via 3D, 10-node, quadratic tetrahedron elements; C3D10 in ABAQUS element library). The modulus of the material was set to be  $E = 10$  GPa, according to the typical values obtained in nanoindentation measurements. The base of the element was fixed and a uniform pressure applied to different regions. Convergence pre-analysis was applied to estimate the required mesh parameters.

**Optical and Electron Microscopy:** Microscopic studies were carried out using optical microscopy (Digital Microscope, Leica DVM6) and electron scanning microscopy (SEM, Jeol JSM7500F). Imaging in SEM was performed using a secondary electron detector at an accelerating voltage of 5 kV.

**XRD/SAXS and XRF Mapping:** Whole claws were carefully glued on a pin sample holder and were measured at the dedicated station for scanning SAXS/WAXS/XRF of the μ-Spot beamline at the BESSY II storage ring (HZB: Helmholtz Center Berlin for Materials and Energy). A beam energy of 15 keV (wavelength,  $\lambda = 0.0826$  nm) was selected for using a multilayered monochromator. The beam was focused on the sample with the aid of toroidal mirror, and the final beam size was defined by a pinhole, 10 μm in diameter, installed before the sample. Diffraction data were obtained using a large-area 2D charge-coupled device (CCD) detector (MarMosaic 225, Mar USA Evanston, USA) situated ≈380 mm away from the sample. For simultaneous XRF measurements, an energy

dispersive detector (ASAS-SDD, KETEK, Germany) was positioned at  $\approx 60^\circ$  to the X-ray beam axis. The sample-to-detector distance was calibrated using quartz X-ray diffraction patterns. For radial and azimuthal integration and reduction of the 2D images into profiles, the software DPDAK was used. For each XRD pattern, the fiber degree of co-alignment was calculated within the range of  $q = 1.2\text{--}1.3\text{ nm}^{-1}$  after radial integration. A normalized width of fitted peaks in azimuthal space was used as a parameter for the relative degree of fiber co-alignment in the sampled scattering volume throughout the claw. The obtained minimal peak width, attributed to the poorly oriented fibers, was set to zero and the obtained maximal width was set to one, representing the highly co-aligned fibers. In order to plot the vector diagram, the fiber-packing SAXS peak and the normalized fiber co-alignments were used. The length of each vector is related to the fraction of aligned fibers, and its orientation represents the orientation of the fibers' long axes. In order to determine the fiber packing density and volume fraction of chitin crystals, hexagonal close packing was assumed. Given the diameter of chitin fibrils,  $D$ , which is typically  $\approx 3\text{ nm}$  and the spacing of the adjacent chitin crystals,  $d$ , obtained from SAXS data analysis, elementary trigonometry was used to calculate the local chitin content.<sup>[8e]</sup>

$$\phi_c = \frac{\pi}{2\sqrt{3}} \left(\frac{D}{d}\right)^2 \quad (1)$$

**Compositional Analysis by EDS and WDS:** EDS and WDS measurements were conducted on carbon coated samples, following nanoindentation or nanowear probing. EDS mapping was performed in a field-emission-gun SEM (FESEM, Jeol JSM 7500F), equipped with two X-ray detectors and a silicon-drift detector (SDD) (Oxford Instruments, UK) and operated by AZtech Software. In these measurements, an accelerated voltage of 20 keV and working distance of 8 mm were used.

Quantitative EDS and WDS measurements with standards were carried out in Technion-Israel Institute of Technology (Haifa, Israel). EDS measurements were performed using a X-Max energy dispersive spectrometer (Oxford Instruments, England) attached to a ZEISS Ultra Plus high-resolution SEM. The energy resolution of EDS was 127 eV. WDS measurements were conducted with an Oxford Instruments wavelength-dispersive spectrometer attached to a Quanta 200 (FEI, USA) SEM. To find the regions of interest on the samples' surfaces, a number of images were collected using secondary and backscattered electrons. All spectroscopic measurements were performed at an optimal working distance for each electron microscope at accelerated voltage equal 10 keV for EDS and 30 keV for WDS. Characteristic X-ray intensities of the monitored elements were calibrated with the aid of standards listed in Table S1, Supporting Information.

**Amino Acid Analysis:** The air-dried claw was used for amino acid analysis (AAA) by Genaxxon bioscience GmbH using amino acid analyser LC3000. Each sample was supplemented with HCl (600  $\mu\text{L}$ , 6 N), sealed under vacuum ( $<20\text{ mbar}$ ) and hydrolyzed for 96 h at  $110^\circ\text{C}$ . After hydrolysis, samples were dried at  $36^\circ\text{C}$  for 4 h (vacuum centrifuge). Each dried sample was supplemented with Na-Acetate buffer (500  $\mu\text{L}$ , pH = 2.2) for subsequent derivatization and high-pressure liquid chromatography (HPLC; polymeric cation exchange column). Fragmented amino acids were detected by post-column Ninhydrin derivatization at  $125^\circ\text{C}$  and photometric measurement at 570 nm. Data were monitored by the chromatography software ChromStar 6.0. following calibration of the HPLC using a commercial standard (Sigma-Aldrich, A2908).

**X-Ray Absorption Near Edge Structure:** Solid samples, including native and re-substituted spider fangs and claws, using  $\text{MnO}_2$  (Sigma-Aldrich) and  $\text{MnCl}_2 \cdot 4\text{H}_2\text{O}$  (Sigma-Aldrich), were ground to fine powders, mixed with low absorbing KBr powder to avoid self-absorption, and pressed into pellets. Liquid samples were mounted between polyethylene terephthalate foils and frozen using liquid nitrogen.

The Mn and Zn K-edge XANES measurements were carried out at the BM08-GILDA beamline at the European Synchrotron Radiation Facility (ESRF, Grenoble, France). The beamline is equipped with a (311) Si-double-crystal monochromator, working in sagittal focusing geometry and using harmonics suppression mirrors.

The Mn and Zn K-edge XAS signals were measured, keeping the sample at the liquid helium temperature, in fluorescence geometry using a 13-element high purity Ge multichannel detector to selectively measure the Mn  $K\alpha$  or Zn  $K\alpha$  fluorescence intensity. The data collected by each channel were summed up and normalized to the incident intensity, measured using an ionization chamber placed before the sample. Up to four spectra were recorded for each sample and averaged to improve measurement statistics.

X-ray fluorescence maps were collected at the microXAS beamline of the Swiss Light Source (SLS, Paul Scherrer Institute (PSI), Viligen, Switzerland). The X-ray beam with energy of 6.6 keV was focused with a kinoform lens to a spot size of  $1\text{ }\mu\text{m}$ . The sample was moved in plane across the micro-focused beam in steps of  $1\text{ }\mu\text{m}$ . The X-ray fluorescence signal was collected with a Ketek detector with 1 s acquisition time. The claw sections mounted on a copper TEM grid, were measured in cryo conditions. The temperature was maintained at  $-170^\circ\text{C}$  by a stream of cold nitrogen using CryoJet 3, Oxford Systems. After mapping the sample using XRF, XANES spectra were acquired by scanning the incoming beam energy across the Mn K-edge and collecting the Mn  $K\alpha$  fluorescence intensity. Three sections from two claws were measured. Six measurements were carried out in regions with high Mn content and low S content, and six in regions with high Mn and high S content. Data processing including baseline subtraction and normalization and averaging were performed using the Athena software package.<sup>[31]</sup> The edge energy was defined as the first maximum of the first derivative of the XANES data.

**Nanoindentation:** Embedded and finely polished samples were probed mechanically with a Triboindenter TI-950 nanomechanical tester (Hysitron, Minneapolis, MN, USA). The reduced modulus ( $E_r$ ) and hardness ( $H$ ) were measured using a 30 mN standard transducer and a fluid cell cube corner diamond tip (with nominally 50–70 nm radius of curvature). The loading/unloading rate of 100  $\mu\text{N/s}$  with a holding time at peak load of 500  $\mu\text{N}$  for 2 s was used. Load-displacement curves were analyzed toward extraction of reduced modulus,  $E_r$ , and hardness,  $H$ , according to the Oliver and Pharr method.<sup>[32]</sup> A grid of indents was performed over an area of  $120 \times 280\text{ }\mu\text{m}^2$ , which included the entire tip of the claw and the spacing of  $5\text{ }\mu\text{m}$  in both dry and hydrated conditions. The same sample was used for dry and hydrated (fully soaked in water) measurements, however with a  $2.5\text{ }\mu\text{m}$  spacing between adjacent indentation points in both the  $x$ - and  $y$ -directions. Two different preloads, 2 and 5  $\mu\text{N}$ , were used to accurately "sense" the samples surface in dry and hydrated conditions, respectively. The same indentation spacing was used to probe the base of the grapnel-like element and the comb-like elements in hydrated condition. Indentation maps were generated using the Hysitron XYZPlot toolkit.

**Nanowear:** To perform the nanowear test, a standard 2D transducer and a  $1\text{ }\mu\text{m}$  conical diamond tip was used in the Triboindenter tester (TI950, Hysitron, Minneapolis, MN, USA). A 350  $\mu\text{N}$  load was applied over the cross-sectional samples with  $5\text{ }\mu\text{m} \times 5\text{ }\mu\text{m}$  scanning size and 2 Hz sliding rate. Nanowear tests were performed with 30 and 10 sliding cycles for all the regions on the cross-section and on the epicuticular region on the surface of the claw base, respectively. An in situ post-wear SPM (scanning probe microscopy) mode on a larger area was used to image and quantify the mean eroded depth. The topographical maps were later generated using Origin (OriginLab V 9.1, Northampton, MA, USA).

**Data Analysis:** The data were statistically analyzed and plotted using Data Analysis ToolPak (Descriptive Statistics) of Excel software (Microsoft Office) and Origin Pro software (OriginLab, Northampton, MA), respectively. The data are presented as the mean values with standard deviation (SD). Hysitron TriboView software was used for analysis of the SPM data. The AZtech software was used for EDS maps. Over 15 spider claws were used in the entire study.

## Supporting Information

Supporting Information is available from the Wiley Online Library or from the author.

## Acknowledgements

The authors are grateful to the Deutsche Forschungsgemeinschaft for financial support under grant no. PO 1725/7-1. E.Z. thanks the Shore Fund for Advanced Composites (Technion) for partial financial support. The authors thank the Department for Neurobiology at the Vienna University for providing the spider material. The authors thank Birgit Schonert for help in sample preparation. Bulk XANES measurements were performed on BM08-GILDA beamline at the European Synchrotron Radiation Facility (ESRF), Grenoble, France. Micro-focused XANES measurements were performed at the microXAS beamline at the Swiss Light Source, at the Paul Scherrer Institut (PSI), Viligen, Switzerland. Microtomography measurements were performed at the BAMline imaging beamline of BESSY II storage ring (HZB: Helmholtz Center Berlin for Materials and Energy). The authors are grateful to Francesco d'Acapito from the GILDA beamline (ESRF), Dr. Daniel Grolimund and Dr. Dario Ferreira Sanchez from the microXAS beamline (SLS, PSI), Ralf Britzke and Dr. Bernd Müller from the BAMline (Bessy II, HBZ) for technical support and providing invaluable beamtime assistance. The authors thank ESRF, SLS, and HZB for the allocation of synchrotron radiation beamtime. Special thanks to Dr. Sergey Kapisnikov for helping with the SLS beamtime and sample preparation, to Clara Valverde Serrano and Hanna Leemreize for help during beamtime at ESRF and SLS.

## Conflict of Interest

The authors declare no conflict of interest.

## Author Contributions

M.T. and Y.P. designed the research and experiments; M.T., O.Y.-M., and Y.P. conducted microscopic, structural, and compositional and spectroscopic experiments; M.T. performed all mechanical experiments and analysis; P.Z. performed and analyzed microtomography data; Y.S., A.R., and B.B.-O. conducted FEA; A.B. and E.Z. conducted WDS and quantitative EDX; all authors contributed to the discussion of the results; M.T. and Y.P. designed the figures and wrote the manuscript with input from all other authors.

## Keywords

abrasion resistance, biopolymers, metal-ion cross-linking, microstructure, tribological behavior

Received: January 15, 2020

Revised: April 30, 2020

Published online: June 25, 2020

- [1] a) J. W. C. Dunlop, P. Fratzl, *Annu. Rev. Mater. Res.* **2010**, *40*, 1; b) M. Eder, S. Amini, P. Fratzl, *Science* **2018**, *362*, 543; c) J. F. V. Vincent, U. G. Wegst, *Arthropod Struct. Dev.* **2004**, *33*, 187.
- [2] a) J. F. V. Vincent, *Composites, Part A* **2002**, *33*, 1311; b) D. Klocke, H. Schmitz, *Acta Biomater.* **2011**, *7*, 2935; c) U. Cerkvénik, B. van de Straat, S. W. S. Gussekloo, J. L. van Leeuwen, *Proc. Natl. Acad. Sci. U. S. A.* **2017**, *114*, E7822; d) Y. Politi, M. Priewasser, E. Pippel, P. Zaslansky, J. Hartmann, S. Siegel, C. H. Li, F. G. Barth, P. Fratzl, *Adv. Funct. Mater.* **2012**, *22*, 2519.
- [3] Y. Song, Z. Dai, Z. Wang, A. Ji, S. N. Gorb, *Sci. Rep.* **2016**, *6*, 26219.
- [4] a) J. Blackwell, M. A. Weih, *J. Mol. Biol.* **1980**, *137*, 49; b) G. Fraenkel, K. M. Rudall, *Proc. R. Soc. Med.* **1947**, *134*, 111; c) C. Valverde Serrano, H. Leemreize, B. Bar-On, F. G. Barth, P. Fratzl, E. Zolotoyabko, Y. Politi, *J. Struct. Biol.* **2016**, *193*, 124.
- [5] Y. Bouligand, *Tissue Cell* **1972**, *4*, 189.
- [6] F. G. Barth, *Z. Zellforsch. Microsk. Anat.* **1973**, *144*, 409.
- [7] S. L. Young, M. Chyasnachyus, M. Erko, F. G. Barth, P. Fratzl, I. Zlotnikov, Y. Politi, V. V. Tsukruk, *Acta Biomater.* **2014**, *10*, 4832.
- [8] a) U. Cerkvénik, J. L. van Leeuwen, A. Kovalev, S. N. Gorb, Y. Matsumura, S. W. S. Gussekloo, *J. Exp. Biol.* **2019**, *222*, 195628; b) M. Erko, M. A. Hartmann, I. Zlotnikov, C. Valverde Serrano, P. Fratzl, Y. Politi, *J. Struct. Biol.* **2013**, *183*, 172; c) M. Erko, O. Younes-Metzler, A. Rack, P. Zaslansky, S. L. Young, G. Milliron, M. Chyasnachyus, F. G. Barth, P. Fratzl, V. Tsukruk, I. Zlotnikov, Y. Politi, *J. R. Soc., Interface* **2015**, *12*, 20141111; d) C. F. Schaber, S. Flenner, A. Glisovic, I. Krasnov, M. Rosenthal, H. Stieglitz, C. Krywka, M. Burghammer, M. Muller, S. N. Gorb, *J. R. Soc., Interface* **2019**, *16*, 20180692; e) Y. Politi, B. Bar-On, H.-O. Fabritius, in *Architected Materials in Nature and Engineering* (Eds: Y. Estrin, Y. Bréchet, J. Dunlop, P. Fratzl), Springer International Publishing, Cham, Switzerland **2019**, p. 287; f) H. O. Fabritius, A. Ziegler, M. Friak, S. Nikolov, J. Huber, B. H. Seidl, S. Ruangchai, F. I. Alagboso, S. Karsten, J. Lu, A. M. Janus, M. Petrov, L. F. Zhu, P. Hemzalova, S. Hild, D. Raabe, J. Neugebauer, *Bioinspiration Biomimetics* **2016**, *11*, 055006.
- [9] a) B. Bar-On, F. G. Barth, P. Fratzl, Y. Politi, *Nat. Commun.* **2014**, *5*, 3894; b) Y. Politi, E. Pippel, A. C. Licuco-Massouh, L. Bertinetti, H. Blumtritt, F. G. Barth, P. Fratzl, *Arthropod Struct. Dev.* **2017**, *46*, 30.
- [10] a) C. C. Broomell, R. K. Khan, D. N. Moses, A. Miserez, M. G. Pontin, G. D. Stucky, F. W. Zok, J. H. Waite, *J. R. Soc., Interface* **2007**, *4*, 19; b) C. C. Broomell, M. A. Mattoni, F. W. Zok, J. H. Waite, *J. Exp. Biol.* **2006**, *209*, 3219; c) H. Birkedal, R. K. Khan, N. Slack, C. Broomell, H. C. Lichtenegger, F. Zok, G. D. Stucky, J. H. Waite, *ChemBioChem* **2006**, *7*, 1392; d) R. M. S. Schofield, M. H. Nesson, K. A. Richardson, P. Wyeth, *J. Insect Physiol.* **2003**, *49*, 31; e) B. W. Cribb, A. Stewart, H. Huang, R. Truss, B. Noller, R. Rasch, M. P. Zalucki, *Naturwissenschaften* **2007**, *95*, 17; f) H. C. Lichtenegger, T. Schoberl, J. T. Ruokolainen, J. O. Cross, S. M. Heald, H. Birkedal, J. H. Waite, G. D. Stucky, *Proc. Natl. Acad. Sci. U. S. A.* **2003**, *100*, 9144; g) H. C. Lichtenegger, T. Schoberl, M. H. Bartl, H. Waite, G. D. Stucky, *Science* **2002**, *298*, 389; h) T. Schoberl, I. L. Jäger, *Adv. Eng. Mater.* **2006**, *8*, 1164; i) T. D. Morgan, P. Baker, K. J. Kramer, H. H. Basibuyuk, D. L. J. Quicke, *J. Stored Prod. Res.* **2003**, *39*, 65; j) D. L. J. Quicke, P. Wyeth, J. D. Fawke, H. H. Basibuyuk, J. F. V. Vincent, *Zool. J. Linn. Soc.* **1998**, *124*, 387; k) B. W. Cribb, A. Rathmell, R. Charters, R. Rasch, H. Huang, I. R. Tibbetts, *Arthropod Struct. Dev.* **2009**, *38*, 173.
- [11] a) S. Amini, A. Miserez, *Acta Biomater.* **2013**, *9*, 7895; b) E. Degtyar, M. J. Harrington, Y. Politi, P. Fratzl, *Angew. Chem., Int. Ed.* **2014**, *53*, 12026.
- [12] a) E. V. Gorb, S. N. Gorb, *Entomol. Exp. Appl.* **2002**, *105*, 13; b) S. N. Gorb, *Attachment Devices of Insect Cuticle*, Springer, The Netherlands **2001**; c) S. N. Gorb, R. G. Beutel, E. V. Gorb, Y. Jiao, V. Kastner, S. Niederegger, V. L. Popov, M. Scherge, U. Schwarz, W. Votsch, *Integr. Comp. Biol.* **2002**, *42*, 1127; d) B. N. J. Persson, S. Gorb, *J. Chem. Phys.* **2003**, *119*, 11437.
- [13] J. Speck, F. G. Barth, *J. Comp. Physiol. A* **1982**, *148*, 187.
- [14] F. P. Beer, E. R. Johnston, J. T. DeWolf, *Mechanics of Materials*, McGraw Hill, New York **1981**.
- [15] a) F. G. Barth, *Z. Zellforsch. Microsk. Anat.* **1969**, *97*, 137; b) F. G. Barth, *Z. Zellforsch. Microsk. Anat.* **1970**, *104*, 87.
- [16] a) S. O. Andersen, M. G. Peter, P. Roepstorff, *Comp. Biochem. Physiol. Part B: Biochem. Mol. Biol.* **1996**, *113*, 689; b) A. Miserez, D. Rubin, J. H. Waite, *J. Biol. Chem.* **2010**, *285*, 38115; c) J. F. V. Vincent, S. Ablett, *J. Insect Physiol.* **1987**, *33*, 973.
- [17] C. C. Broomell, F. W. Zok, J. H. Waite, *Acta Biomater.* **2008**, *4*, 2045.

- [18] F. W. Zok, A. Miserez, *Acta Mater.* **2007**, *55*, 6365.
- [19] a) A. B. Kesel, A. Martin, T. Seidl, *J. Exp. Biol.* **2003**, *206*, 2733; b) J. O. Wolff, S. N. Gorb, *Sci. Rep.* **2013**, *3*, 1101.
- [20] V. L. Popov, in *Contact Mechanics and Friction*, Springer, Berlin **2010**, p. 271.
- [21] A. C. Neville, *Q. J. Microsc. Sci.* **1965**, *106*, 315.
- [22] J. M. Gosline, P. A. Guerette, C. S. Ortlepp, K. N. Savage, *J. Exp. Biol.* **1999**, *202*, 3295.
- [23] a) H. Zhao, J. H. Waite, *Biochemistry* **2006**, *45*, 14223; b) M. G. Pontin, D. N. Moses, J. H. Waite, F. W. Zok, *Proc. Natl. Acad. Sci. U. S. A.* **2007**, *104*, 13559; c) C. C. Broomell, S. F. Chase, T. Laue, H. J. Waite, *Biomacromolecules* **2008**, *9*, 1669.
- [24] D. N. Moses, M. G. Pontin, J. H. Waite, F. W. Zok, *Biophys. J.* **2008**, *94*, 3266.
- [25] a) U. G. K. Wegst, M. F. Ashby, *Philos. Mag.* **2004**, *84*, 2167; b) M. F. Ashby, *Materials Selection in Mechanical Design*, Elsevier Science, Amsterdam, The Netherlands **2016**.
- [26] A. Miserez, Y. Li, J. H. Waite, F. Zok, *Acta Biomater.* **2007**, *3*, 139.
- [27] A. P. Jackson, J. F. V. Vincent, R. M. Tunner, *Proc. R. Soc. Lond. B Biol. Sci.* **1988**, *234*, 415.
- [28] Z. Xu, *Sci. Rep.* **2013**, *3*, 2914.
- [29] N. Holten-Andersen, M. J. Harrington, H. Birkedal, B. P. Lee, P. B. Messersmith, K. Y. Lee, J. H. Waite, *Proc. Natl. Acad. Sci. U. S. A.* **2011**, *108*, 2651.
- [30] E. Filippidi, T. R. Cristiani, C. D. Eisenbach, J. H. Waite, J. N. Israelachvili, B. K. Ahn, M. T. Valentine, *Science* **2017**, *358*, 502.
- [31] B. Ravel, M. Newville, *J. Synchrotron Radiat.* **2005**, *12*, 537.
- [32] W. C. Oliver, G. M. Pharr, *J. Mater. Res.* **1992**, *7*, 1564.